

Constraining the Stellar Mass Function from the Deficiency of Tidal Disruption Flares in the Nuclei of Massive Galaxies

Daniel J. D’Orazio^{1*}, Abraham Loeb¹, James Guillochon¹

¹*Astronomy Department, Harvard University, 60 Garden Street, Cambridge, MA 02138*

7 April 2024

ABSTRACT

The rate of tidal disruption flares (TDFs) per mass of the disrupting black hole encodes information on the present-day mass function (PDMF) of stars in the clusters surrounding super massive black holes. We explore how the shape of the TDF rate with black hole mass can constrain the PDMF, with only weak dependence on black hole spin. We show that existing data can marginally constrain the minimum and maximum masses of stars in the cluster, and the high-mass end of the PDMF slope, as well as the overall TDF rate. With $\mathcal{O}(100)$ TDFs expected to be identified with the Zwicky Transient Facility, the overall rate can be highly constrained, but still with only marginal constraints on the PDMF. However, if $\lesssim 10\%$ of the TDFs expected to be found by LSST over a decade ($\mathcal{O}(10^3)$ TDFs) are identified, then precise and accurate estimates can be made for the minimum stellar mass (within a factor of two) and the average slope of the high-mass PDMF (to within $\mathcal{O}(10\%)$) in nuclear star clusters. This technique could be adapted in the future to probe, in addition to the PDMF, the local black hole mass function and possibly the massive black hole binary population.

Key words: stars: luminosity function, mass function – galaxies: nuclei

1 INTRODUCTION

A star can be ripped apart by a supermassive black hole (BH) when the tidal force across the star exceeds the gravitational force that binds the star. Depending on the relative sizes and masses of the star and BH, this can occur before, or after the star plunges across the BH event horizon. If disruption occurs outside of the event horizon, we may observe the event as a tidal disruption flare (TDF, *e.g.*, Hills 1975; Rees 1988; Gezari et al. 2006, 2009; van Velzen et al. 2011; Bloom et al. 2011; Gezari et al. 2012; Chornock et al. 2014; Arcavi et al. 2014; Holoien et al. 2014; Vinkó et al. 2015; Tadhunter et al. 2017), else the event is likely dark or significantly different in appearance, (*e.g.* D’Orazio & Levin 2013; D’Orazio et al. 2016; Lu et al. 2017).

Recently van Velzen (2018, hereafter V18) estimated the rate of TDFs per mass of the disrupting BH and showed a steep drop in TDF rate above $M_* \sim 10^8 M_\odot$, approximately the BH mass above which the disruption of a $1 M_\odot$ star is hidden from observation behind the BH horizon. Because the measured BH mass function does not drop off as steeply as this TDF mass function, V18 takes this finding as evidence for a horizon, and the validity of the TDF hypothesis for events identified as such.

Here we show that this fall-off not only demonstrates the existence of a horizon, but also encodes rich information on the present day stellar mass function (PDMF) in the nuclear star clusters surrounding super massive BHs. This is because the properties of the

star that is being disrupted directly affects the properties of the resultant TDF, and thus the population of TDFs represents the underlying population of stars that is being disrupted.

We use the volumetric rate of TDFs to constrain the mass function of stars in the nuclear clusters surrounding super massive BHs. This is determined by the shape of the rate distribution with BH mass, not its overall normalization, which depends on the number of stars prone to disruption in addition to the details of stellar dynamics (Magorrian & Tremaine 1999; Wang & Merritt 2004; Stone & Metzger 2016). Specifically, we exploit the relation between the tidal radius scale and the BH event horizon scale to predict the minimum stellar mass that can be disrupted outside the horizon of a BH of specified mass. Because the PDMF sets the number of stars above a certain mass, the TDF rate per BH mass encodes the shape of the PDMF.

Using a sample of 12 TDFs with BH mass measurements from V18, and generating a new sample of 17 TDFs by combining the V18 dataset with the dataset from Mockler et al. (2018, hereafter M18), we marginally constrain the low mass and high mass cutoffs for stars in the PDMF, $M_{\min} = 0.93^{+5.7}_{-0.85} M_\odot$ and $M_{\max} = 43.0^{+105.0}_{-33.0} M_\odot$; an average metallicity of stars in the nuclear cluster, $\log_{10}(Z/Z_\odot) = 0.94^{+0.88}_{-0.94}$, and using a broken power for the PDMF, we constrain the high-mass PDMF slope of $\xi = -1.6^{+1.0}_{-2.0}$, with very little sensitivity to the BH spin. The PDMF and the above parameters are defined below in Eq. (6).

While the existing data does not provide significant constraints on the PDMF, we find that the precision on at least the minimum stellar mass and the slope of the PDMF will improve by an order

* daniel.dorazio@cfa.harvard.edu

of magnitude in the LSST era, when $\gtrsim 10^3$ identified TDFs will be available. Hence, the novel technique presented here would prove powerful in constraining the PDMF within galactic nuclei, where intriguing evidence indicates top-heavy IMFs (e.g., Bartko et al. 2010) and high metallicities (e.g., Do et al. 2018).

In § 2 we present our analytic calculation of the conditional probability for measuring a specific BH mass given the observation of a TDF. In § 3 we present constraints on the PDMF from present and expected future observations of the BH-mass dependent TDF rate. In § 4 we discuss possible improvements to this model and conclude.

2 METHODS

We calculate the probability that a galaxy’s central super massive BH has a mass M_\bullet given that a TDF is observed in that galaxy. This probability can be written via Bayes’ theorem as,

$$\mathcal{P} \equiv P(M_\bullet | \text{TDF}) = \frac{P(\text{TDF} | M_\bullet) P(M_\bullet)}{P(\text{TDF})}. \quad (1)$$

We are interested in the shape of this probability distribution as a function of M_\bullet . With this in mind, we assume that $P(\text{TDF})$ is a constant that encodes the overall normalization of the rate at which stars are delivered onto orbits that will be captured by super massive BHs and result in a TDF. This term could have a weak dependence on BH mass (Brockamp et al. 2011; Wang & Merritt 2004; Kochanek 2016; Stone & Metzger 2016), a feature we plan to explore in future work. For $P(M_\bullet)$, we choose the local BH mass function of Shankar et al. (2004). Hence, we are left with calculating the likelihood term in the numerator of Eq. (1): the conditional probability that a star will be disrupted, given knowledge of the BH mass.

2.1 Probability of a TDF given the BH mass

A star with mass M_* and radius r_* will be disrupted if it passes within a distance (Hills 1975),

$$r_T = \left(\frac{M_\bullet}{M_*} \right)^{1/3} r_*, \quad (2)$$

of a black hole of mass M_\bullet . If the BH mass is too large, or the star is too tightly bound, the disruption will occur inside the event horizon of the BH. No TDF will be observed when $r_T \geq r_{\text{ibco}}$, where,

$$r_{\text{ibco}} = \frac{GM_\bullet}{c^2} \left[2 \mp \mathcal{S} + 2\sqrt{1 \mp \mathcal{S}} \right], \quad (3)$$

is the inner-most-bound circular orbit (IBCO) of the BH in the equatorial plane (Bardeen et al. 1972; Levin & Perez-Giz 2009), which depends on the BH mass and spin, \mathcal{S} .¹ Inside of this radius the star will plunge into the BH.

Because the value of r_{ibco} is different for prograde and retrograde stellar orbits (ranging from GM/c^2 for $\mathcal{S} = 1$ to $(3 + 2\sqrt{2})GM/c^2$ for $\mathcal{S} = -1$), we assume that there is no preference for stellar angular momentum relative to BH spin and take the average value,

$$\langle r_{\text{ibco}} \rangle_{\mathcal{S}} = \frac{GM_\bullet}{c^2} \left[2 + \sqrt{1 - \mathcal{S}} + \sqrt{1 + \mathcal{S}} \right]. \quad (4)$$

¹ We are not aware of any analytic expression for the general angle dependent IBCO for arbitrary spin (Hod 2017; Will 2012).

This quantity is always larger than the horizon radius and has a smaller spin dependent range than the horizon radius. This is a consequence of including retrograde orbits which will cause the star to be captured at a much larger radius without disruption. For a single interaction, r_{ibco} changes the radius at which a star will be swallowed before disruption by a large amount, a factor of almost 6 between maximally spinning prograde and retrograde orbits. When averaging over many interactions, however, the spin of the BH does not have a large effect, statistically, on the disruption of an infalling star. It will, however, contribute to an intrinsic scatter in the rate.

Note that, for simplicity, we average the spin dependent value of the IBCO only over equatorial prograde and retrograde orbits. This choice yields the maximal spin dependence of the IBCO. This is because the spin dependence of the IBCO becomes weaker for orbits inclined away from the equatorial plane (Will 2012). That is, averaging over the entire sphere of encounters would result in an averaged IBCO with an even weaker dependence on the spin than found in Eq. (4), with a range more tightly constrained to $4GM/c^2$.

To solve for the critical stellar mass, M_{crit}^* , above which disruption by a BH of given mass may occur, we must adopt a stellar mass-radius relation. Here we provide a simple fitting function to the main-sequence, metallicity-dependent mass-radius relation of Tout et al. (1996) that matches well observational data for metallicities $Z/Z_\odot \in (0.03, 3)$,

$$\log_{10} \left[\frac{r_*(M_*, Z)}{r_\odot} \right] = \min \left\{ \log_{10} \left[0.85 \left(\frac{M_*}{M_\odot} \right)^{0.85} \right], 0 \right\} + \max \left\{ \log_{10} \left[\left(\frac{Z}{Z_\odot} \right)^{0.096} \left(\frac{M_*}{M_\odot} \right)^{0.60} \right], 0 \right\}. \quad (5)$$

Assuming $Z = Z_\odot$, we can solve analytically for the critical mass (see Appendix). Otherwise we find M_{crit}^* by numerically solving expression (2) for M_* when $r_T = \langle r_{\text{ibco}} \rangle_{\mathcal{S}}$ and with r_* given by Eq. (5).

The probability that a star, on a trajectory towards the BH tidal disruption radius, will disrupt outside of the event horizon is the same as the probability that this star is above the critical mass M_{crit}^* . This probability can be derived from a model of the PDMF. We assume a PDMF proportional to a Kroupa initial-stellar-mass function (IMF) with a parameterized slope above $0.5M_\odot$,

$$\frac{dN_*}{dM_*} \propto H(M_* - M_{\text{min}}) [1 - H(M_* - M_{\text{max}})] \times \begin{cases} C_1 \left(\frac{M_*}{M_\odot} \right)^{-0.3} & M_* < 0.08M_\odot, \\ C_2 \left(\frac{M_*}{M_\odot} \right)^{-1.3} & 0.08M_\odot \leq M_* \leq 0.5M_\odot, \\ \left(\frac{M_*}{M_\odot} \right)^\xi & M_* > 0.5M_\odot, \end{cases} \quad (6)$$

$$C_1 = (0.5M_\odot)^{\xi+1.3}, \quad C_2 = \frac{C_1}{0.08M_\odot},$$

and with lower and upper stellar mass cutoffs M_{min} and M_{max} , and where the constants C_1 and C_2 ensure that the power law breaks occur at the correct value of M_* . H is the Heaviside function.

The probability of a disruption, given the BH mass, is then,

$$P(\text{TDF} | M_\bullet) \equiv P(M_* \geq M_{\text{crit}} | M_\bullet) = \frac{\int_{M_{\text{crit}}^*}^{\infty} \frac{dN_*}{dM_*} dM_*}{\int_0^{\infty} \frac{dN_*}{dM_*} dM_*}. \quad (7)$$

Combining (5)–(7), we find an analytic expression for $P(\text{TDF} | M_\bullet)$ in terms of the numerically derived value of M_{crit} (for a simplified analytical form of M_{crit} , see the Appendix). This

allows us to compute the desired quantity, $P(M_{\bullet}|\text{TDF})$ in Eq. (1). Because we are only interested in the shape of $P(M_{\bullet}|\text{TDF})$ with M_{\bullet} , we choose $P(\text{TDF}) = 1/K_0$ by which the overall rate is normalized.

2.2 Parameter dependencies

We plot the derived TDF rate $P(M_{\bullet}|\text{TDF})$ in Figure 1 for various BH spins, stellar metallicities, and PDMFs, varying the cutoff masses M_{\min} and M_{\max} as well as the high-mass slope of the PDMF. We use fiducial parameter values of $(M_{\min}, M_{\max}, \mathcal{S}, \xi, Z) = (0.01M_{\odot}, 10M_{\odot}, 0, -2.35, Z_{\odot})$ unless otherwise stated in the figure legends. As a reference we plot in grey the data for the TDF rate from V18.

All of the realizations of the BH mass dependent TDF rate in Figure 1 show the same general behavior. For lower BH masses, there is a shallow decrease in the TDF rate with BH mass that follows the BH mass function $P(M_{\bullet})$. For higher BH masses, there is a steep cutoff in the rate. The cutoff marks where stars drawn from the prescribed PDMF are no longer favored to be above the critical mass for disruption. The main effect of changing the PDMF and BH spin is to change the shape and location of this cutoff.

The top left panel of Figure 1 shows the change in the TDF rate as a function of BH spin. The teal lines depict the TDF rate when considering direction-averaged stellar orbits relative to the BH spin. This amounts to using the spin-direction averaged value of r_{ibco} presented in Eq. (4), valid for averaging many TDFs. The result implies very little spin dependence with a small preference for higher spin BHs to allow higher disruption rates at higher BH masses (associated with a shift of the cutoff to higher BH masses).

For reference, the grey shaded region in the top left panel shows the range of TDF rates possible for all values of the spin, *i.e.*, the bounds of the shaded region correspond to the rates expected for purely retrograde or purely prograde stellar orbits around a maximally spinning BH. This indicates that a large scatter in the BH spin dependent TDF rate is expected; however, for a large number of TDFs, the average rate will converge to a result with very little spin dependence. This scatter is a tracer of the range of BH spin magnitudes in the sample.

The left panel also shows that a change in the spin, even if not averaging over spin direction, affects the TDF rate uniformly with BH mass, shifting the curve horizontally for different values of the spin. As we now see from the remaining panels in Figure 1, this is a very different change in the rate than the shape change that results from varying the PDMF parameter values.

The bottom left panel of Figure 1 shows the change in the TDF rate as a function of the maximum stellar mass, M_{\max} . Increasing the maximum allowed stellar mass extends the TDF rate to higher values at high BH masses. This is because higher mass main-sequence stars are less tightly bound (Eq. 5) and can thus be disrupted by higher mass BHs (see Eq. 2).

The purple lines in the bottom left panel of Figure 1 show the effect of changing stellar metallicity, which has a similar effect as changing the maximum mass. Higher metallicity stars above $1M_{\odot}$ are less tightly bound (see Tout et al. 1996, and Eq. 5). Hence, higher metallicity stars can be more easily disrupted at higher BH masses. We consider metallicity as high as those presented in Figure 1 because there is evidence for high metallicity stellar populations (up to $10Z_{\odot}$) in galactic nuclear star clusters (Do et al. 2018). When fitting to data, however, we use more conservative constraints on Z for consistency with the metallicity with which the mass-radius relation is calibrated.

The top right panel of Figure 1 shows the change in the TDF rate as a function of the minimum stellar mass, M_{\min} . Increasing M_{\min} , for a fixed M_{\max} , narrows the range of possible stellar masses and hence steepens the TDF rate cutoff at high BH mass. The minimum stellar mass does not change the value of the maximum disrupting BH mass, as is the case for M_{\max} . Instead, the value of M_{\min} crucially changes the shape of the cutoff by changing the range of stellar masses available for disruption; the fraction of stars with mass above the critical mass for disruption drops quickly when M_{\min} and M_{\max} are close in value, while the cutoff is more gradual for disparate values of M_{\min} and M_{\max} .

The bottom right panel of Figure 1 shows the change in the TDF rate as a function of the high-mass slope of the PDMF, ξ . Steeper values of the high-mass PDMF slope imply a lower fraction of high-mass stars and hence a lower probability of disruption at higher BH masses. A steeper slope also boosts the relative number of low mass stars. As a result, the effect of a steeper PDMF slope on the mass dependent TDF rate is similar to that found for decreasing M_{\min} in the top left panel of Figure 1.

In summary, the maximum stellar mass and the metallicity (M_{\max}, Z) set the BH mass above which no TDFs occur. The minimum stellar mass and the high-mass PDMF slope (M_{\min}, ξ) set the shape of the cutoff. The direction-averaged BH spin has very little influence on the BH mass dependent TDF rate, but could encode the range of spin magnitudes in the scatter of TDF rates.

3 APPLICATION TO PRESENT AND FUTURE DATA

We fit our model to two data sets: the data in Figure 3 of V18 (available in the online version) and to an extended data set that we have constructed using BH masses measured directly from the TDF light curve (M18). We then fit our model to mock data that could be gathered in the ZTF and LSST eras.

3.1 van Velzen and Mockler data sets

The construction of the V18 TDF volumetric rate per BH mass is presented in V18. To construct the M18 data set, we used the maximum volume method outlined in V18. For the BH masses, we use the union of the van Velzen and M18 BH masses, using the mass from M18 if the TDF is represented in both sets. For the quantity z_{\max} we use only the value derived from the survey flux limit and the peak TDF flux (namely, the value in Table 1 of V18).

We use both data sets and our model to constrain the mass function of stars in galactic nuclei. To this goal we construct the likelihood that our model $\mathcal{P}(M_{\bullet}; \Theta)$ with parameters Θ is the correct model given the data $(p_i, M_{\bullet,i})$. Because the data is not constructed from a simple binning across BH masses, but rather is constructed with uncertainties in both coordinates we construct a log-likelihood function that can take into account errors in both coordinates. We generalize the one-dimensional χ^2 to higher dimensions, which cannot be done uniquely because of a choice for how to compute the distance between a model and a data point. We choose to compute the minimum distance between point and model. This results in choosing the line that orthogonally intersects the model.

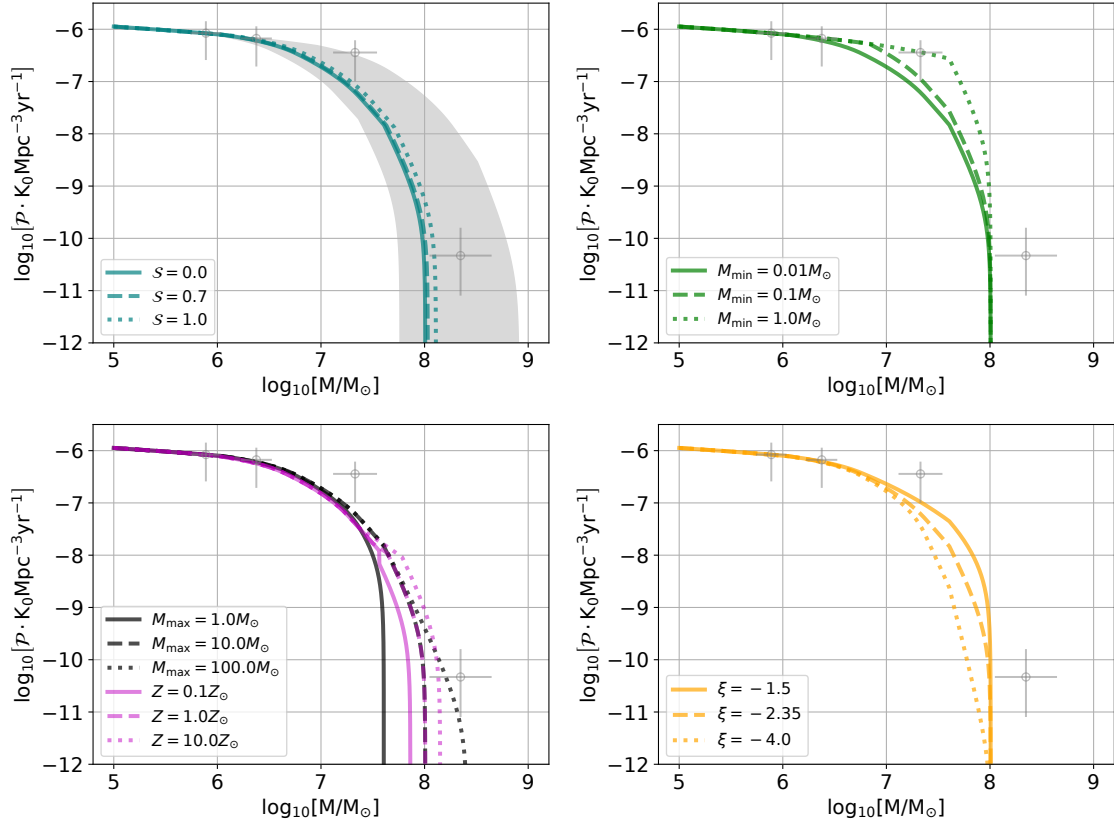


Figure 1. Model parameter dependencies. From top left to bottom right, the varied parameters are the dimensionless BH spin, S ; the minimum stellar mass, M_{\min} ; the maximum stellar mass, M_{\max} , (black) and metallicity, Z (purple); and the high-mass slope of the PDMF ξ . The grey shaded region in the top left panel is the range of values taken if the spin *direction* is not averaged. The grey data points are from van Velzen (2018) for reference.

This log likelihood is written

$$\begin{aligned}
 -\ln \mathcal{L} &= \sum_i \frac{\left(\log_{10} p_i - \log_{10} \left[\mathcal{P}_i(M_{\bullet,i}^{\text{proj}}; \Theta) \right] \right)^2}{2\sigma_{\log_{10} p_i}^2} \\
 &+ \frac{\left(\log_{10} M_{\bullet,i}^{\text{obs}} - \log_{10} M_{\bullet,i}^{\text{proj}} \right)^2}{2\sigma_{\log_{10} M_{\bullet,i}}^2}, \quad (8)
 \end{aligned}$$

where $M_{\bullet,i}^{\text{proj}}$ is the solution to the minimization of the distance between data point and model for a given set of model parameters, *i.e.*, the x -coordinate for which a line between the data point and the model is the shortest. Summation is over the i^{th} data point. The quantities $\sigma_{\log_{10} p_i}^2$ and $\sigma_{\log_{10} M_{\bullet,i}}^2$ are the one-standard deviation uncertainties on the i^{th} data point. In addition to the parameters, $\Theta = (M_{\min}, M_{\max}, S, \xi, Z)$, we also vary the normalization constant K_0 with units of $\text{Mpc}^{-3} \text{yr}^{-1}$.

We use the dynamic nested sampling code `Dynesty` (Spiegel *et al. in prep.*)², based on the algorithm of Higson *et al.* (2017), to sample the posterior distribution. We assume uniform priors given in Table 1. For both the V18 and M18 data sets we present the median posterior values along with the parameter range that falls within the 16th and 84th quantiles in Table 2.

We find similar results for both data sets. The best fit parameter values are displayed in Table 2. The results of fitting to the V18

Table 1. The ranges of the uniform priors used for nested sampling. Here K_* is a constant that equals $10^{-4.125}$ for the V18 and M18 runs, and equals the true value of the normalization for the Mock-data runs.

Parameter	Bounds
$\log_{10} [M_{\min}/M_{\odot}]$	$[-2.0, 2.0]$
$\log_{10} [M_{\max}/M_{\odot}]$	$[-2.5, 2.5]$
S	$[0.0, 1.0]$
ξ	$[-5.0, 0.0]$
$\log_{10} [Z/Z_{\odot}]$	$[-2.45, 0.45]$
$\log_{10} [K_0]$	$K_* \pm 1.0$

data are displayed in Figure 2 while the results from fitting to the M18 data are displayed in Figure 3. Each figure shows the 16th-84th-quantile (dark teal) and 5th-95th-quantile (light teal) ranges of highest likelihood models to the data (left panel) and corner plot representations of the 1D and 2D posteriors (right panel). Note that the posteriors are not all Gaussian. This is apparent in the location of the 16th and 84th quantiles of each 1D posterior distribution denoted by the vertical dashed lines in the corner plots.

While the V18 and M18 data sets are sparse, the data points at the highest BH masses define the position and shape of the rate cutoff sufficiently to place a wide, but not flat, constraint on the model parameter values. In the text below we quote numbers from the M18 analysis, though the V18 numbers are similar.

- M_{\min} : On the high end, the minimum stellar mass is not sig-

² <http://dynesty.readthedocs.io/en/latest/>

Table 2. The median-likelihood model parameter values, $\Theta(\mathcal{L}_{\text{med}})$, given the TDF rate per BH mass data from Figure 3 of van Velzen (2018) and the data generated in this work from a combined sample of BH masses from Mockler et al. (2018) and van Velzen (2018). Parameter uncertainties are quoted at 16th and 84th percentile values corresponding to 1σ uncertainties for Gaussian errors.

Parameter	$[\Theta(\mathcal{L}_{\text{med}})_{-84\%}^{+16\%}]$	
	V18 Best Fit Values (Fig. 2)	M18 Best Fit Values (Fig. 3)
M_{min}/M_{\odot}	$1.1_{-1.0}^{+10.4}$	$0.93_{-0.85}^{+5.7}$
M_{max}/M_{\odot}	47_{-37}^{+108}	43_{-33}^{+105}
\mathcal{S}	--	--
ξ	$-2.3_{-1.7}^{+1.6}$	$-1.6_{-2.0}^{+1.0}$
$\log_{10}(Z/Z_{\odot})$	$-0.88_{-0.96}^{+0.88}$	$-0.94_{-0.94}^{+0.88}$
$\log_{10} K_0$	$-4.12_{-0.14}^{+0.14}$	$-4.45_{-0.11}^{+0.12}$

Table 3. The same as Table 2, but for the two sets of mock data displayed in Figure 4. For convenience, the mock data is generated with a value of the normalization K_0 that is different than in the case of the real data.

Parameter	Truth Values	$[\Theta(\mathcal{L}_{\text{med}})_{-84\%}^{+16\%}]$	
		$N = 400$	$N = 4 \times 10^3$
M_{min}/M_{\odot}	1.0	$3.2_{-2.8}^{+15.0}$	$1.7_{-0.6}^{+1.6}$
M_{max}/M_{\odot}	70.0	65_{-46}^{+109}	155_{-86}^{+176}
\mathcal{S}	0.7	--	--
ξ	-2.0	$-1.3_{-2.0}^{+0.9}$	$-2.0_{-0.3}^{+0.3}$
$\log_{10}(Z/Z_{\odot})$	0.0	$-0.8_{-1.0}^{+0.8}$	$-0.6_{-0.9}^{+0.6}$
$\log_{10} K_0$	-1.60	$-1.60_{-0.02}^{+0.02}$	$-1.60_{-0.01}^{+0.01}$

nificantly constrained. The median likelihood value is $0.9M_{\odot}$ and only 16% of the likelihood favors $M_{\text{min}} \leq 0.1M_{\odot}$, possibly suggesting preference for a minimum stellar mass $\gtrsim 0.1M_{\odot}$.

- M_{max} : The median likelihood value of the maximum stellar mass is $43M_{\odot}$ and ranges from $10M_{\odot}$ up to $148M_{\odot}$, for the 16% and 84% quantiles. Any value in this range should be taken as a lower limit for the maximum stellar mass. This is because M_{max} can only truly be probed if the observed disruptions require such a high-mass star. These disruptions are rare, the rarity of which depends on the PDMF slope ξ . The more TDFs observed, the higher the chance that high-stellar-mass disruptions could be found. Hence the lower limit on M_{max} will increase with additional TDFs until its true value will be tightly constrained.

- \mathcal{S} : The BH spin is not constrained. This is because we use the retrograde/prograde averaged value of r_{ibco} to denote the point of no return for an infalling star (Eq. 4). As shown in Figure 1, this results in very little dependence of our model on the BH spin. As noted below Eq. (4), we expect this insensitivity to be robust as our expression for the average radius of the IBCO is a conservative choice, allowing maximum spin dependence. Note that the fall-off

in posterior probability (right panels of Figures 2 and 3) for the spin at high and low values, is due to smoothing of the posterior, resulting in an artificial drop in probability at the prior boundaries. Hence the labeled constraints $\mathcal{S} = 0.5_{-0.3}^{+0.3}$ in Figures 2 and 3 are artificial. In the next section we show that there is still no spin dependence even when considering a sample of 4×10^3 TDFs.

We note, however, that the spin averaging that we invoke is only valid when each BH mass bin contains many more than a single TDF. As the V18 and M18 data sets have bins with 1 or 2 TDFs, this assumption breaks down. One can think of these small number bins as requiring larger y-error bars than shown due to a random draw of BH spin in the range $[-1, 1]$.

- ξ : The PDMF slope above $0.5M_{\odot}$ is not well constrained but prefers shallow, top-heavy values, pushing up against the prior limit of $\xi = 0$.

- Z/Z_{\odot} : The average metallicity of the stellar population is consistent with solar, but also prefers high values, and like the PDMF slope, pushes up against the prior value of $3Z_{\odot}$.

From the corner plots in both Figures 2 and 3, one can see that there is a degeneracy in M_{min} and ξ . This degeneracy is already suggested by Figure 1; both M_{min} and ξ affect the shape of the rate cutoff at intermediate BH masses. This degeneracy can, however, be removed in future data sets with more data for TDFs caused by BHs in the mass range $\log_{10}(M/M_{\odot}) \sim 7.5 - 8$.

The main differences in the results from the V18 and the M18 data sets is the reduced degeneracy between M_{min} and ξ . This is because of the extra TDF directly at the knee of the TDF-rate cutoff in the M18 data. This leads to an even higher estimate for M_{min} , and a slightly lower estimate for ξ (Table 2). Recall, however, that this difference is due to only one TDF.

In the next section we show definitively that more data points at higher BH masses do indeed remove the $M_{\text{min}}-\xi$ degeneracy.

3.2 Constraints from the ZTF and LSST

The Zwicky Transient Facility (ZTF), which has recently been commissioned, could detect 10 – 70 TDFs per year (Hung et al. 2017). The Large Synoptic Survey Telescope (LSST; Ivezić & et al. 2008) is expected to discover 4×10^3 TDFs per year (van Velzen et al. 2011), starting in the 2020s. Because the BH mass can be measured directly from the TDF lightcurve itself (M18), it will be possible to build a TDF BH mass function for hundreds of events in the ZTF era and thousands of events in the LSST era. While identifying TDFs is difficult, methods involving photometric cuts and spectroscopic follow-up, when feasible, have proven effective (e.g. Hung et al. 2017). Here we create mock samples of TDFs and associated BH masses based on an optimistic ZTF scenario/pessimistic LSST scenario (400 TDFs) and an expected LSST scenario (4×10^3 TDFs).

For each mock data set, we choose a truth model and randomly sample N draws from this distribution. We bin these draws into \sqrt{N} evenly sized mass bins with y error given by the \sqrt{N} Poisson estimate. To generate the probability distribution from which we draw, we normalize Eq. (7) by the integral over Eq. (7) from $10^5 M_{\odot}$ to infinity.

To fit to the binned data, we use a Poisson likelihood,

$$-\ln \mathcal{L} = \sum_i \log N_i! + \mu_i - N_i \log \mu_i, \quad (9)$$

where N_i is the number of counts in the i^{th} mass bin, and the model expectation value for the number of counts in a bin of size ΔM is

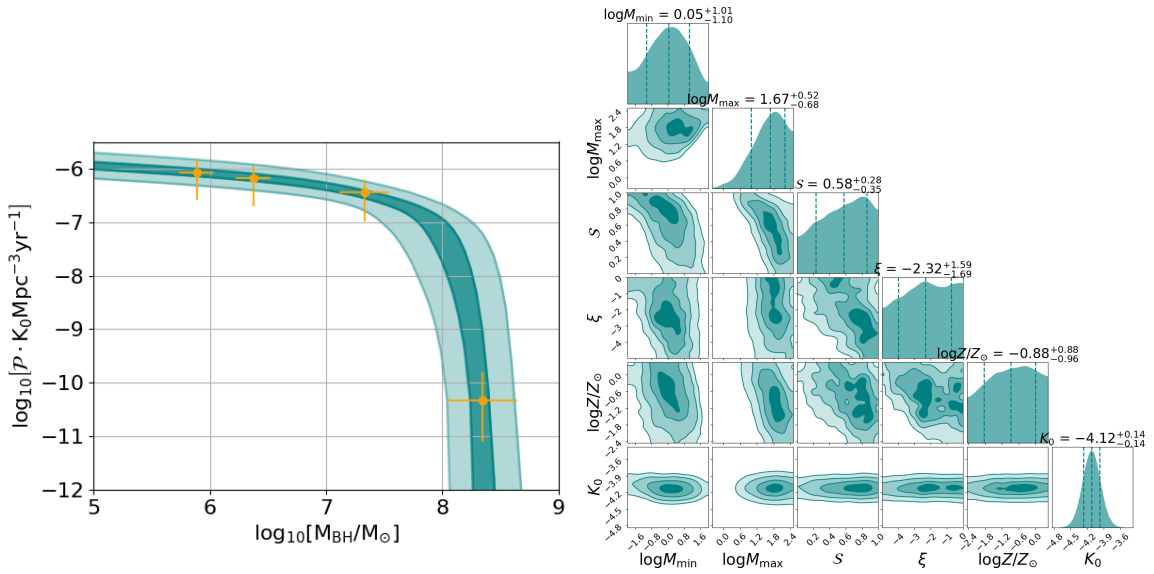


Figure 2. *Left:* Orange points with error bars are the derived volumetric rates of TDFs taken from [van Velzen \(2018\)](#). The shaded dark (light) teal region represents the 16th-84th quantile (5th-95th quantile) range of the highest likelihood models, Eq. (7). *Right:* Corner plot showing 2D and 1D representations of the posterior distribution. The vertical lines on each 1D posterior distribution represent the 16th, 50th, and 84th quantiles from left to right. With the small number of TDFs in this present data set, the PDMF is not well constrained, however, these constraints will improve greatly in the LSST era, as shown in Figure 4.

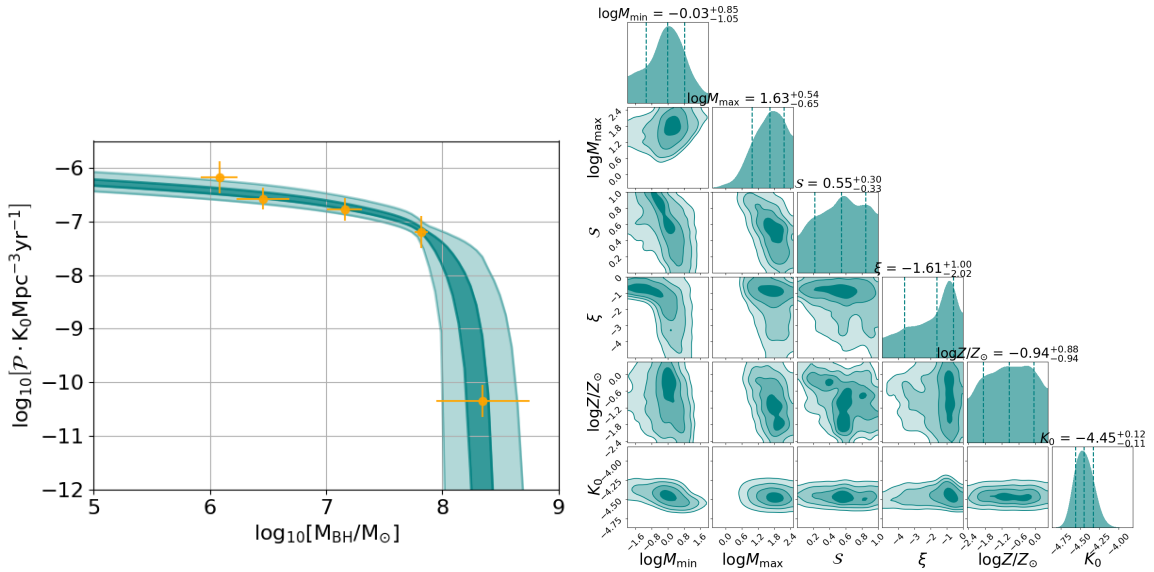


Figure 3. The same as Figure 2, but for the data set derived from the union of the [van Velzen \(2018\)](#) and [Mockler et al. \(2018\)](#) data sets as described in § 3.1. The numbers of TDFs in the five bins are [3,8,4,1,1]. From the small number of TDFs in existing data, the PDMF is not well constrained, however, these constraints will improve greatly in the LSST era, as shown in Figure 4.

$\mu_i \equiv N_{\text{tot}} \tilde{\mathcal{P}}_i \Delta M$, given the normalized probability $\tilde{\mathcal{P}}_i$ at the center of the mass bin and the total number of events N_{tot} . In practice we approximate $\log N! \approx N \log N - N + 1/2 \log \pi(2N + 1/3)$, which agrees with the exact expression to at least the third decimal place for all N . We again use the `Dynesty` code to sample the posterior distribution and recover the best fit parameter values and error bars. The assumed priors are listed in Table 1.

The two scenarios considered here represent an optimistic scenario at the end of ZTF and the beginning of LSST ($N = 400$), and an expected LSST scenario ($N = 4 \times 10^3$). For 10 years of an

LSST-like survey, these correspond to 1% and 10% of all transients classified as TDFs purely from their lightcurves.

The best fit parameter values and the underlying truth values are tabulated in Table 3. The results of fitting to both mock data sets are displayed in Figure 4. The top row displays results for the ZTF ($N = 400$) scenario and the bottom row displays results for the LSST ($N = 4 \times 10^3$) scenario. The right column of Figure 4 shows the 1D and 2D posteriors from a combined ensemble of 10 different random draws from the underlying truth distribution, while the left column shows one of these realizations (orange data points) as

well as the true underlying model (dashed red) and the 16th-84th quantile and 5th-95th quantile uncertainties (black and grey shaded regions) from the parameter recovery. In the right panels, the truth values are indicated by red lines. We find that the truth values can be recovered well for both data sets.

In both scenarios, the normalization parameter K_0 is recovered very well simply because most of the TDFs fall at low BH mass where the normalization is set. As in the real data sets, the BH spin parameter is again unconstrained for both the ZTF and LSST scenarios.

We find only a moderate enhancement in parameter constraints from the present day data to the ZTF ($N = 400$) scenario. For example, the ZTF mock data exhibits the same degeneracy between M_{\min} and ξ and has only slightly smaller 16th-84th quantile error bars (see Tables 2 and 3). In the ZTF scenario, however, the overall rate normalization is now precisely constrained to within $\mathcal{O}(1\%)$ as opposed to $\mathcal{O}(10\%)$ with the present day data.

Moving to the LSST scenario, we find a large improvement in parameter recovery accuracy and constraints for the M_{\min} and ξ parameter values. The constraint on the metallicity is only moderately improved, while the constraint on the maximum mass is largely unchanged from the ZTF scenario.

For M_{\min} and ξ , the 16th-84th-quantile error bars are reduced by almost an order of magnitude. More interestingly the degeneracy between the two is removed and the PDMF slope ξ is recovered accurately and precisely. While M_{\min} is recovered more precisely, and still consistently, it is overestimated in both the ZTF and LSST scenarios.

The large improvement in parameter recovery between the ZTF ($N = 400$) and LSST ($N = 4 \times 10^3$) scenarios suggests that $N \gtrsim 10^3$ is the target number of TDFs needed to make meaningful constraints on the PDMF, especially the PDMF slope ξ and the minimum stellar mass M_{\min} . An even greater number of TDFs are needed to probe the maximum stellar mass if it is of order the fiducial value of $70M_{\odot}$ chosen here. This is expected, however, because the rarest events, involving the disruption of the most massive stars by the most massive BHs, constrain the maximum stellar mass. We discuss this further in the next section.

4 DISCUSSION AND CONCLUSIONS

We have shown that the BH mass dependent TDF rate can provide constraints on the PDMF of stars in galactic nuclei. In particular, one can constrain the minimum and maximum stellar mass, the high-mass slope of the PDMF, and the average stellar metallicity. For a large enough sample of TDFs, the BH spin enters through the scatter in the TDF mass dependent rate, an analysis of which we leave for the future.

Fitting to existing data, consisting of 17 TDFs for which a BH mass can be estimated, provides a preliminary demonstration of the constraining power of this method. Our best fit parameter values and 16th-84th-quantile uncertainties are recorded in Table 2. While the uncertainties on the best fit parameter values are large, we find reasonable values for the PDMF model parameters.

Fitting to mock data relevant for the end of the ZTF era shows that the overall TDF rate can be constrained to within $\mathcal{O}(1\%)$, however, the PDMF is still only marginally constrained with 400 TDFs (see the top row of Figure 4 and Table 3).

Fitting to mock data relevant for the LSST era, consisting of 4×10^3 confirmed TDFs, which corresponds to identification of only 10% of expected TDFs over a 10 year LSST lifetime, we find

that the minimum stellar mass in the cluster can be constrained within a factor of two for an assumed $1M_{\odot}$ truth value, and that the high-mass PDMF slope can be constrained to of order ± 0.3 . A lower limit can be placed on the maximum stellar mass in the cluster (see the bottom row of Figure 4 and Table 3).

Most of the constraining power originates from observations of TDFs with high-mass BHs. As discussed in §2.2, this is because the rate of TDFs generated by low mass BHs reflect only the BH mass function. TDFs generated by BHs approaching a few times $10^7 M_{\odot}$ hold information on the minimum stellar mass and the PDMF slope. TDFs generated by $\sim 10^8 M_{\odot}$ BHs determine the maximum stellar masses and the metallicity. However, the high-information content TDFs from the highest mass BHs are more rare and hence, statistically, require a larger sample of TDFs to gather. This is the main reason why a larger sample of TDFs is required to constrain the PDMF.

We note, however, that when generating mock data, we do not assume any dependence of TDF luminosity on stellar or BH mass. If, however, TDFs disrupted by more massive BHs, for example, are intrinsically brighter, then the volume within which they can be observed is larger compared to TDFs associated with less massive BHs. The result being that our mock data under-samples the number of TDFs that would be associated with the more massive BHs. Hence, our estimate of the constraining power of the TDF rate is conservative. Note that this is only an issue when generating mock data, the real data of course take this into account via the maximum-volume method used in v18.

This point is indeed hinted at by the existence of the ASASSN-15lh TDF. This event defines the high BH mass cutoff in the TDF rate and influences the fits to the PDMF model displayed in Figures 2 and 3. Within the model, however, such an event is highly improbable and such events only begin to appear in the LSST mock data. For the fiducial PDMF parameter values, and assuming uniform intrinsic luminosity across the BH mass spectrum, the ASASSN-15lh event is an approximately one in 10^4 event. However, because ASASSN-15lh is $\sim \times 10$ brighter than other TDFs, the volume of observation is increased by a factor of 10^3 , making ASASSN-15lh more like a one in 10 event.

Note that, the ASASSN-15lh event, while important for determining the cutoff in TDF rate at high BH mass, mostly provides information only on the maximal mass for the analysis of the V18 and M18 data. Removing the ASASSN-15lh data point from the analysis, we find that the recovered parameter values and uncertainties are not significantly altered. The largest excursion is for the maximum stellar mass estimate, decreasing in median value and increasing in range to $25_{-22}^{+120} M_{\odot}$ ($32_{-27}^{+127} M_{\odot}$ for the M18 data) as opposed to $47_{-37}^{+108} M_{\odot}$ ($43_{-33}^{+105} M_{\odot}$ for the M18 data) when ASASSN-15lh is included. The minimum stellar mass estimate changes to $0.6_{-0.5}^{+7.5} M_{\odot}$ ($1.0_{-0.9}^{+5.3} M_{\odot}$ for the M18 data) compared to $1.1_{-1.0}^{+10.4} M_{\odot}$ ($0.93_{-0.85}^{+5.7} M_{\odot}$ for the M18 data) when ASASSN-15lh is included. The other parameters stay nearly the same with only small increases in the 16th-84th-quantile uncertainties. This suggests that ASASSN-15lh may be more important for signifying a cutoff in the rate and motivating the TDF model than it is for constraining the PDMF, at least at the level of detail present in the V18 and M18 data sets. We suspect that when more data in the knee of the differential TDF rate function is populated, the inclusion of ASASSN-15lh could have a larger effect on the accuracy of the recovered parameters.

The probability and influence of an ASASSN-15lh event aside, we note that one should be cautious when considering only a single TDF at the high BH mass end of the TDF rate function.

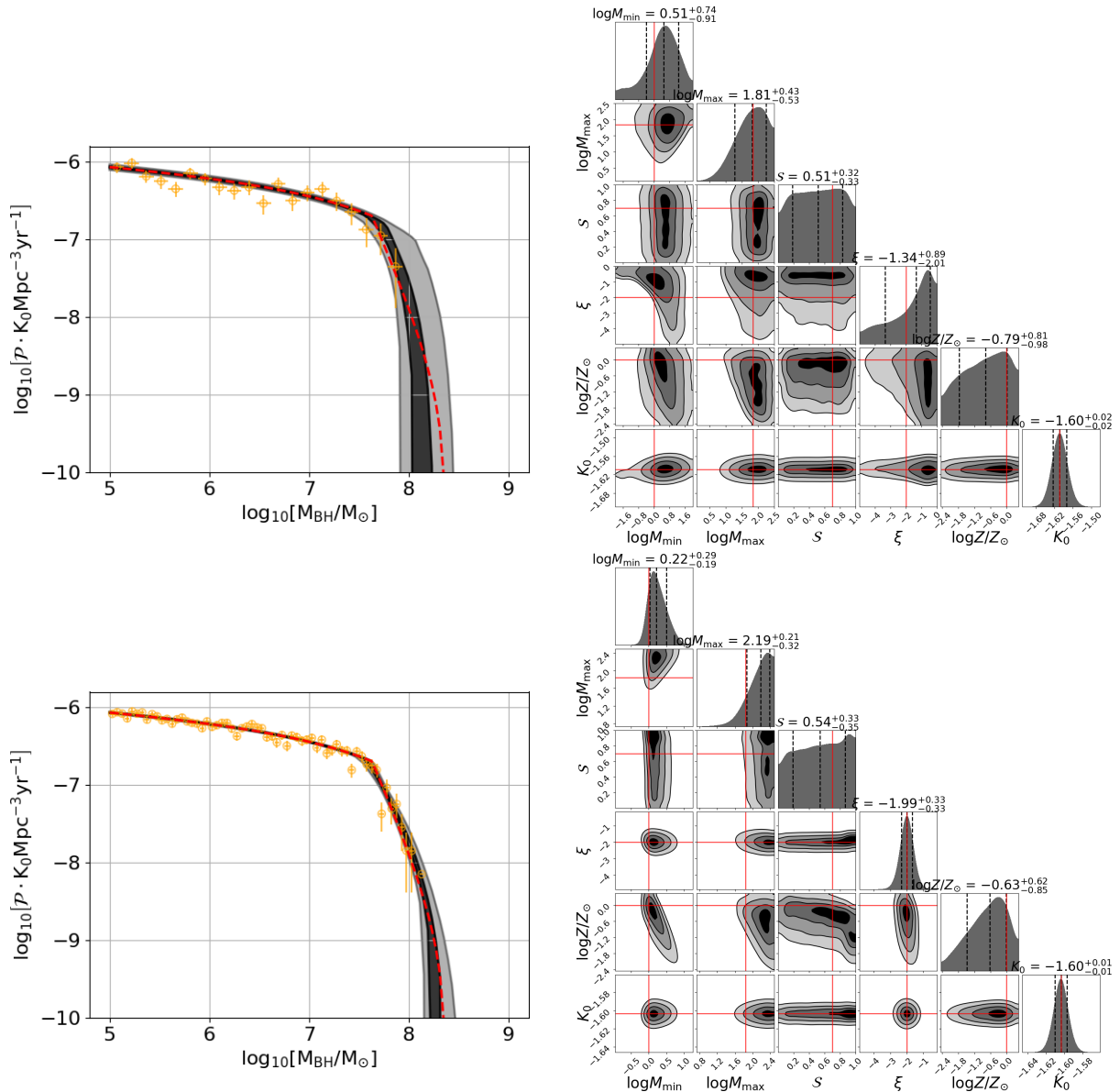


Figure 4. The same as Figures 2 and 3, but for mock data for 400 TDFs (top row) and 4×10^3 TDFs (bottom row), inspired by the number of TDFs that could be identified by the ZTF and by the yearly rate expected for LSST respectively. The assumed parameter values (truth values), from which the data are drawn are indicated by red lines in the right panels. The true model is shown as a dashed red line in the left panels.

It could be that ASASSN-15lh is not due to the tidal disruption of a star at all (e.g., Dong et al. 2016; Metzger et al. 2015; Sukhbold & Woosley 2016; Margutti et al. 2017; Krühler et al. 2018). That possibility aside, even if ASASSN-15lh is a bona-fide TDF, its location in the existing data could be skewed a few different ways. One possibility is that this event is the result of a highly spinning BH (e.g., Leloudas et al. 2016). Because the highest BH mass bin consists only of the single ASASSN-15lh data point, we could be prone to a larger uncertainty than reflected by the Poissonian error bars. Future additions to the TDF rate will determine the extent to which ASASSN-15lh is an outlier.

Another interesting possibility is that ASASSN-15lh is the product of a disruption by a compact, super massive BH binary with a disparate mass ratio (Coughlin & Armitage 2018), thereby allowing a large central BH mass measurement, yet disruption by

a much smaller BH. The possibility of this scenario depends on the unknown probability of finding a super massive BH binary at a given separation (e.g., Haiman et al. 2009; D’Orazio et al. 2015), compared to the probability of observing such a disruption, computed here. That is, what is more improbable: the chance of finding a TDF from such a large BH, out of a sample of $\mathcal{O}(10)$; or, the chance of finding a super massive BH binary with the required mass ratio in a range of orbital separations small enough to not alter the BH mass measurement, but large enough to not alter the TDF light curve.

For a super massive BH binary with an orbital period on order the TDF timescale, the TDF lightcurve may hold clues to its binary origin, or perhaps it would not be recognizable at all (Hayasaki & Loeb 2016; Coughlin et al. 2017; Liu et al. 2014; Vigneron et al. 2018). It would be interesting to consider at what level a super

massive BH binary population could effect the BH mass-dependent TDF rate (e.g., [Fragione & Leigh 2018](#)) and include this as a factor into the model presented here.

Interpretation of the BH mass dependent TDF rate could also be affected by the presence of a different mass-radius relation than adopted here, e.g., involving the disruption of a non-main sequence star such as a red giant. This, however, would likely cause a discernibly different TDF (e.g. [MacLeod et al. 2013](#)). While red giants and other non-main sequence stars make up only a small fraction ($\lesssim 10\%$) of the stellar population, a large enough TDF sample may begin to identify non-main sequence star disruptions. In that case the analysis presented here, but adapted to the different stellar species, could serve as an additional constraint on the PDMF probed through main-sequence disruptions.

In summary, we have demonstrated a novel technique for constraining the PDMFs of nuclear star clusters from tidal disruptions of stars by massive BHs and also presented the most up to date version of the differential TDF rate per BH mass using the BH masses of TDFs from both V18 and M18. We conclude with a number of additional caveats and topics for future exploration.

- *BH spin*: The range of BH spins could generate an intrinsic scatter in the TDF rate. (see also v18 for discussion of spin inference from the BH mass dependent TDF rate).

- *Metallicity range*: The mass to radius relation the we use for main sequence stars, derived from the fit of ([Tout et al. 1996](#)), breaks down for metallicities above $\sim 3Z_{\odot}$. However, there is observational evidence for higher metallicity environments in the Galactic Centre ([Do et al. 2018](#)). Note further that non-main sequence stars, or stars with pericentre just larger than the tidal disruption radius, may have a different mass-to radius relation entirely (e.g. [MacLeod et al. 2013](#)), regardless of metallicity.

- *Redshift dependence*: One could introduce a differential TDF with redshift as well as BH mass by binning the TDFs in redshift. With enough TDFs (approximately the number of redshift bins times the numbers quoted in each analysis of this work), this would allow one to track the redshift evolution of the stellar mass function that might be expected from, e.g., redshift dependent metallicity evolution ([Belczynski et al. 2016](#)).

- *TDF rate cutoff at low BH mass*: If the TDF luminosity is limited by the Eddington luminosity of the BH ([De Colle et al. 2012](#)), or if the local BH mass function drops off due to the absence of intermediate mass BHs ($10^4 - 10^5 M_{\odot}$), then the BH-mass dependent TDF rate should drop off also at small BH masses. An Eddington-limited observational bias could be included in future analyses of the TDF rate in order to investigate the low end of the BH mass function (see also v18 for discussion of the low end of the BH mass function in this context).

- *Dependence on the BH mass function*: As a related point, we have used a single BH mass function and not allowed the values of the parameters determining this to vary. With the many future TDFs expected at lower BH masses, future data could also constrain the local BH mass function in a higher dimensional parameter space version of the analysis presented here.

- *Form of the model PDMF*: For clarity, we have presented our analysis for only one class of PDMF model, namely a broken power law. Future analyses could also examine the ability to select between model classes (e.g. power law vs. exponential cutoff), or introduce a more general PDMF model.

- *Stellar mass preference for disruption?*: In using the TDF rate to constrain the PDMF, we assume that there is no preference for a given mass star to be on a disrupting orbit. If there is preference for

a subset of stellar masses to be perturbed onto centrophilic orbits, then the work here is constraining the mass function only of those stars.

- *Generation of BH mass dependent TDF rate*: When creating the binned data in Figure 3, we opted to choose bin sizes that reproduce the data from V18. However, the bin choice is somewhat arbitrary. This will likely not be an issue once the number of TDFs increases in the LSST era, but if more information is to be gleaned from the existing data, the effects of bin size should be explored. Alternatively, one might abandon binning entirely and fit to a cumulative distribution function rather than the probability distribution function used here.

The exploration of each of the above items would prove useful for developing a powerful new tool for probing the unique stellar environments surrounding super massive BHs in the centers of galactic nuclei.

ACKNOWLEDGEMENTS

The authors thank Brenna Mockler, Ben Johnson, Rebecca Oppenheimer, Will Farr, Josh Spiegel, and Sjoert van Velzen for useful comments, discussions, and information. DJD thanks Norm Murray for his talk at the Black Hole Initiative that inspired this work. The authors thank the anonymous referee for an insightful review that improved the quality of this manuscript. Financial support was provided from NASA through Einstein Postdoctoral Fellowship award number PF6-170151 (DJD). This work was supported in part by the Black Hole Initiative, which is funded by a grant from the John Templeton Foundation.

APPENDIX A: ANALYTIC EXPRESSION FOR SOLAR-METALLICITY, SALPETER MASS FUNCTION MODELS

Setting $Z = Z_{\odot}$, and using only a single power law (Salpeter) mass function, the probability \mathcal{P} (Eq. 1) can be written analytically in a simple expression. We include it here for use in cursory estimates of the BH mass dependent TDF rate

For $Z = Z_{\odot}$, the main-sequence mass-radius relation is approximated as,

$$r_* = \left(\frac{M_*}{M_{\odot}}\right)^{\xi} r_{\odot}, \quad \text{where} \quad \begin{cases} \xi = 0.85 & M \leq M_{\odot} \\ \xi = 0.6 & M > M_{\odot} \end{cases}.$$

Then the critical mass is

$$M_{\text{crit}}(\xi) \equiv \left[\left(\frac{\langle r_{\text{ibco}} \rangle_{\mathcal{S}} M_{\odot}}{M_{\bullet} r_{\odot}} \right)^3 M_{\odot}^{(3\xi-3)} M_{\bullet}^2 \right]^{1/(3\xi-1)}, \quad (\text{A1})$$

which we write as,

$$M_{\text{crit}}^* = \text{Max} \{ M_{\text{crit}}(0.85), M_{\text{crit}}(0.6) \}, \quad (\text{A2})$$

to take into account the change in mass-radius relation on the main sequence.

Assuming a PDMF that is the result of a power law (e.g., Salpeter) initial stellar mass function ([Magorrian & Tremaine 1999](#)),

$$\frac{dN_*}{dM_*} \propto \left(\frac{M_*}{M_{\odot}}\right)^{\xi} H(M_* - M_{\text{min}})[1 - H(M_* - M_{\text{max}})], \quad (\text{A3})$$

with lower and upper stellar mass cutoffs M_{\min} and M_{\max} enforced by the Heaviside function H .

Then carrying out the integrals in Eq. (7), we find that in this simplified, but still useful case, the probability of a disruption, given the BH mass, is given by the analytic expression,

$$P(\text{TDF}|M_{\bullet}) = \frac{\{1 - H(M_{\text{crit}}^* - M_{\max})\}}{1 + \xi} \times \quad (\text{A4})$$

$$\left\{ \left[M_{\min}^{1+\xi} - M_{\text{crit}}^{1+\xi} \right] \left[M_{\max}^{1+\xi} - M_{\min}^{1+\xi} + H(M_{\text{crit}}^* - M_{\min}) \right] \right\},$$

which is substituted into Eq. (1) to get \mathcal{P} .

REFERENCES

- Arcavi I., et al., 2014, *ApJ*, **793**, 38
- Bardeen J. M., Press W. H., Teukolsky S. A., 1972, *ApJ*, **178**, 347
- Bartko H., et al., 2010, *ApJ*, **708**, 834
- Belczynski K., Holz D. E., Bulik T., O’Shaughnessy R., 2016, *Nature*, **534**, 512
- Bloom J. S., et al., 2011, *Science*, **333**, 203
- Brockamp M., Baumgardt H., Kroupa P., 2011, *MNRAS*, **418**, 1308
- Chornock R., et al., 2014, *ApJ*, **780**, 44
- Coughlin E. R., Armitage P. J., 2018, *MNRAS*, **474**, 3857
- Coughlin E. R., Armitage P. J., Nixon C., Begelman M. C., 2017, *MNRAS*, **465**, 3840
- D’Orazio D. J., Levin J., 2013, *PRD*, **88**, 064059
- D’Orazio D. J., Haiman Z., Duffell P., Farris B. D., MacFadyen A. I., 2015, *MNRAS*, **452**, 2540
- D’Orazio D. J., Levin J., Murray N. W., Price L., 2016, preprint, ([arXiv:1601.00017](https://arxiv.org/abs/1601.00017))
- De Colle F., Guillochon J., Naiman J., Ramirez-Ruiz E., 2012, *ApJ*, **760**, 103
- Do T., Kerzendorf W., Konopacky Q., Marcinik J. M., Ghez A., Lu J. R., Morris M. R., 2018, *ApJL*, **855**, L5
- Dong S., et al., 2016, *Science*, **351**, 257
- Fragione G., Leigh N., 2018, *MNRAS*, **479**, 3181
- Gezari S., et al., 2006, *ApJL*, **653**, L25
- Gezari S., et al., 2009, *ApJ*, **698**, 1367
- Gezari S., et al., 2012, *Nature*, **485**, 217
- Haiman Z., Kocsis B., Menou K., 2009, *ApJ*, **700**, 1952
- Hayasaki K., Loeb A., 2016, *Scientific Reports*, **6**, 35629
- Higson E., Handley W., Hobson M., Lasenby A., 2017, preprint, ([arXiv:1704.03459](https://arxiv.org/abs/1704.03459))
- Hills J. G., 1975, *Nature*, **254**, 295
- Hod S., 2017, preprint, ([arXiv:1707.05680](https://arxiv.org/abs/1707.05680))
- Holoien T. W.-S., et al., 2014, *MNRAS*, **445**, 3263
- Hung T., et al., 2017, preprint, ([arXiv:1712.04936](https://arxiv.org/abs/1712.04936))
- Ivezic Z., et al. 2008, preprint, ([arXiv:0805.2366](https://arxiv.org/abs/0805.2366))
- Kochanek C. S., 2016, *MNRAS*, **461**, 371
- Krühler T., et al., 2018, *A&A*, **610**, A14
- Leloudas G., et al., 2016, *Nature Astronomy*, **1**, 0002
- Levin J., Perez-Giz G., 2009, *PRD*, **79**, 124013
- Liu F. K., Li S., Komossa S., 2014, *ApJ*, **786**, 103
- Lu W., Kumar P., Narayan R., 2017, *MNRAS*, **468**, 910
- MacLeod M., Ramirez-Ruiz E., Grady S., Guillochon J., 2013, *ApJ*, **777**, 133
- Magorrian J., Tremaine S., 1999, *MNRAS*, **309**, 447
- Margutti R., et al., 2017, *ApJ*, **836**, 25
- Metzger B. D., Margalit B., Kasen D., Quataert E., 2015, *MNRAS*, **454**, 3311
- Mockler B., Guillochon J., Ramirez-Ruiz E., 2018, preprint, ([arXiv:1801.08221](https://arxiv.org/abs/1801.08221))
- Rees M. J., 1988, *Nature*, **333**, 523
- Shankar F., Salucci P., Granato G. L., De Zotti G., Danese L., 2004, *MNRAS*, **354**, 1020
- Stone N. C., Metzger B. D., 2016, *MNRAS*, **455**, 859
- Sukhbold T., Woosley S. E., 2016, *ApJL*, **820**, L38
- Tadhunter C., Spence R., Rose M., Mullaney J., Crowther P., 2017, *Nature Astronomy*, **1**, 0061
- Tout C. A., Pols O. R., Eggleton P. P., Han Z., 1996, *MNRAS*, **281**, 257
- Vigneron Q., Lodato G., Guidarelli A., 2018, *MNRAS*, **476**, 5312
- Vinkó J., et al., 2015, *ApJ*, **798**, 12
- Wang J., Merritt D., 2004, *ApJ*, **600**, 149
- Will C. M., 2012, *Classical and Quantum Gravity*, **29**, 217001
- van Velzen S., 2018, *ApJ*, **852**, 72
- van Velzen S., et al., 2011, *ApJ*, **741**, 73